nature materials

Article

https://doi.org/10.1038/s41563-022-01393-0

Hierarchically engineered nanostructures from compositionally anisotropic molecular building blocks

Received: 17 April 2021

Accepted: 30 September 2022

Published online: 10 November 2022

Check for updates

Ruiqi Liang[1,7], Yazhen Xue[1,7], Xiaowei Fu[1,2,7], An N. Le[1], Qingliang Song[3], Yicheng Qiang[3], Qiong Xie[3], Ruiqi Dong[4], Zehao Sun[5], Chinedum O. Osuji[4], Jeremiah A. Johnson[5] ✉, Weihua Li[3] & Mingjiang Zhong[1,6] ✉

The inability to synthesize hierarchical structures with independently tailored nanoscale and mesoscale features limits the discovery of next-generation multifunctional materials. Here we present a predictable molecular self-assembly strategy to craft nanostructured materials with a variety of phase-*in*-phase hierarchical morphologies. The compositionally anisotropic building blocks employed in the assembly process are formed by multicomponent graft block copolymers containing sequence-defined side chains. The judicious design of various structural parameters in the graft block copolymers enables broadly tunable compositions, morphologies and lattice parameters across the nanoscale and mesoscale in the assembled structures. Our strategy introduces advanced design principles for the efficient creation of complex hierarchical structures and provides a facile synthetic platform to access nanomaterials with multiple precisely integrated functionalities.

The diverse and complex yet precise functions of living systems benefit substantially from biomolecular self-assembly processes that are regulated across atomic, nanoscopic (~1–100 nm), mesoscopic (~100 nm–1 μm) and macroscopic (>1 μm) length scales. Biomaterials hierarchically assembled from molecular building blocks continuously motivate and inspire the design and fabrication of multifunctional synthetic analogues. Recent success in the development of top-down processing methods advanced the fabrication of macroscopic devices with programmed mesoscopic patterns[1–5]; supramolecular assembly strategies enabled the formation of hierarchical structures endowed with both subnanometre atomic and nanoscale features[6–10]. Nevertheless, strategies that bridge mesoscopic and nanoscopic structures are limited. Control over material structures between the nanoscale and mesoscale is primarily accessed by the bottom-up self-assembly of the nanoparticle[11–14] or (macro)molecular[15–18] building blocks. While a broad spectrum of ordered nanostructures has been constructed, integrating more than one type of ordered nanostructure into a single material with well-arranged and independently sized lattices has been realized only in some rare cases[19–21]. Constructing hierarchically structured bulk materials that combine both nanoscale and mesoscale features in a programmable and scalable manner remains an even greater challenge.

Design and preparation of compositionally anisotropic molecular building blocks

Herein, we present a synthetic platform for the preparation of compositionally anisotropic molecular building blocks (CAMBBs) that can

[1]Department of Chemical and Environmental Engineering, Yale University, New Haven, CT, USA. [2]State Key Laboratory of Polymer Materials Engineering, Polymer Research Institute of Sichuan University, Chengdu, China. [3]State Key Laboratory of Molecular Engineering of Polymers, Department of Macromolecular Science, Fudan University, Shanghai, China. [4]Department of Chemical and Biomolecular Engineering, University of Pennsylvania, Philadelphia, PA, USA. [5]Department of Chemistry, Massachusetts Institute of Technology, Cambridge, MA, USA. [6]Department of Chemistry, Yale University, New Haven, CT, USA. [7]These authors contributed equally: Ruiqi Liang, Yazhen Xue, Xiaowei Fu. ✉e-mail: jaj2109@mit.edu; mingjiang.zhong@yale.edu

https://doi.org/10.1038/s41563-022-01393-0

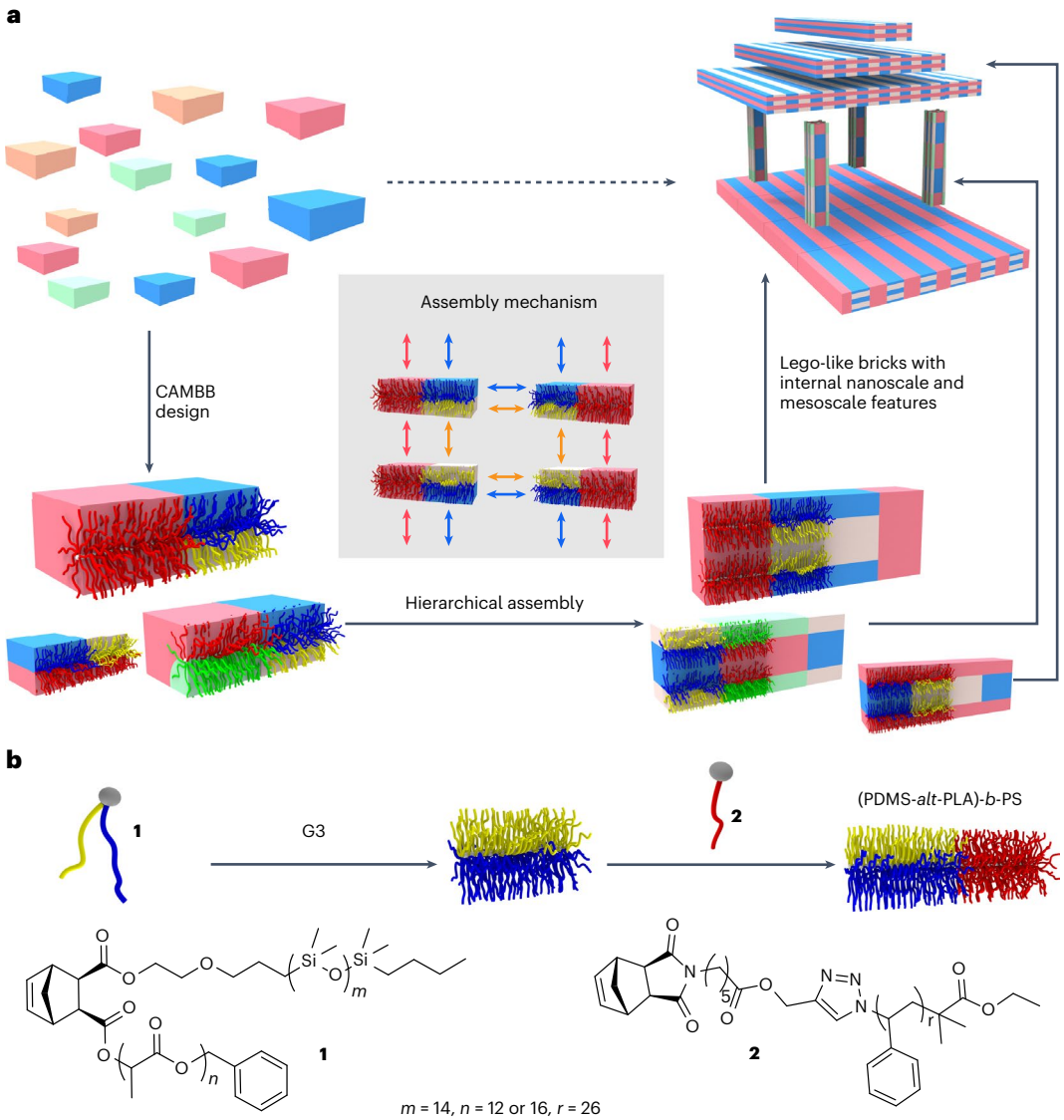

Fig. 1 | Hierarchical nanostructures constructed from GBCP-based CAMBBs. a, A Lego-brick-like molecular construction through the self-assembly of CAMBBs. **b**, Synthetic scheme for the preparation of a representative (A-*alt*-B)-*b*-C-type GBCP: (PDMS-*alt*-PLA)-*b*-PS.

assemble into ordered hierarchical nanostructures (Fig. 1a, bottom). The resulting hierarchical nanostructures can potentially be fabricated into macroscopic devices with well-defined nanoscale and mesoscale features through advanced processing techniques (Fig. 1a, top right). The CAMBBs are based on graft block copolymers (GBCPs) with a rationally designed sequence of side chains. For instance, an (A-*alt*-B)-*b*-C type GBCP was synthesized with the first block containing both side chains A and B tethered to each repeat unit, followed by a second block with side chains C (Fig. 1b). The notation of (A-*alt*-B) indicates that the side chains A and B were arranged in a pseudo-alternating sequence in the first block. The chemical incompatibility of A and B results in intramolecular phase separation of the two types of side chain, creating an interface of A-rich and B-rich nanodomains superimposed on the backbone. The C-containing block that is miscible with neither A nor B generates a second interface with (A-*alt*-B) normal to the backbone. Consequently, the compositional anisotropy directs the CAMBBs to form ordered nanostructures with periodic length scales captured by the characteristic sizes of the CAMBBs, that is, the side chain and backbone lengths of the GBCPs.

The first series of (A-*alt*-B)-*b*-C GBCPs for the proof-of-concept studies contained poly(lactic acid) (PLA), polydimethylsiloxane (PDMS) and polystyrene (PS) as the A, B and C side chains, respectively (Fig. 1b). Ring-opening metathesis polymerization (ROMP) of a norbornene-containing branched macromonomer tethered with PDMS and PLA (**1**, Fig. 1b), referred to as Nb-(PDMS-*branch*-PLA), was initiated by the third-generation Grubbs catalyst (G3)[22] and produced the first block, $(PDMS\text{-}alt\text{-}PLA)_x$, where the subscript x outside of the parentheses stands for the number of the norbornene repeating units, that is, the degree of polymerization of the GBCP backbone. Chain extension of $(PDMS\text{-}alt\text{-}PLA)_x$ was carried out by adding the Nb-PS macromonomer (**2**, Fig. 1b)—a linear PS chain end-functionalized with a norbornene—to form a ternary GBCP of $(PDMS\text{-}alt\text{-}PLA)_x\text{-}b\text{-}(PS)_y$ with y units of Nb-PS integrated. This molecular design was inspired by two previous discoveries: (1) the A-*b*-B-type diblock GBCPs, for example, $(PDMS)_x\text{-}b\text{-}(PS)_y$ and $(PLA)_x\text{-}b\text{-}(PS)_y$, can phase-separate to form ordered nanostructures with nanointerfaces perpendicular to the backbones at the block junctions and a structural periodicity in the range of 20–300 nm (refs. [23–26]); and (2) the A-*alt*-B-type GBCPs, including $(PDMS\text{-}alt\text{-}PLA)_x$, can intramolecularly form a Janus-type biphasic morphology, and further intermolecularly construct ordered nanostructures with the backbones serving as the nanointerfaces and a structural periodicity in the range of 5–30 nm (refs. [27,28]).

https://doi.org/10.1038/s41563-022-01393-0

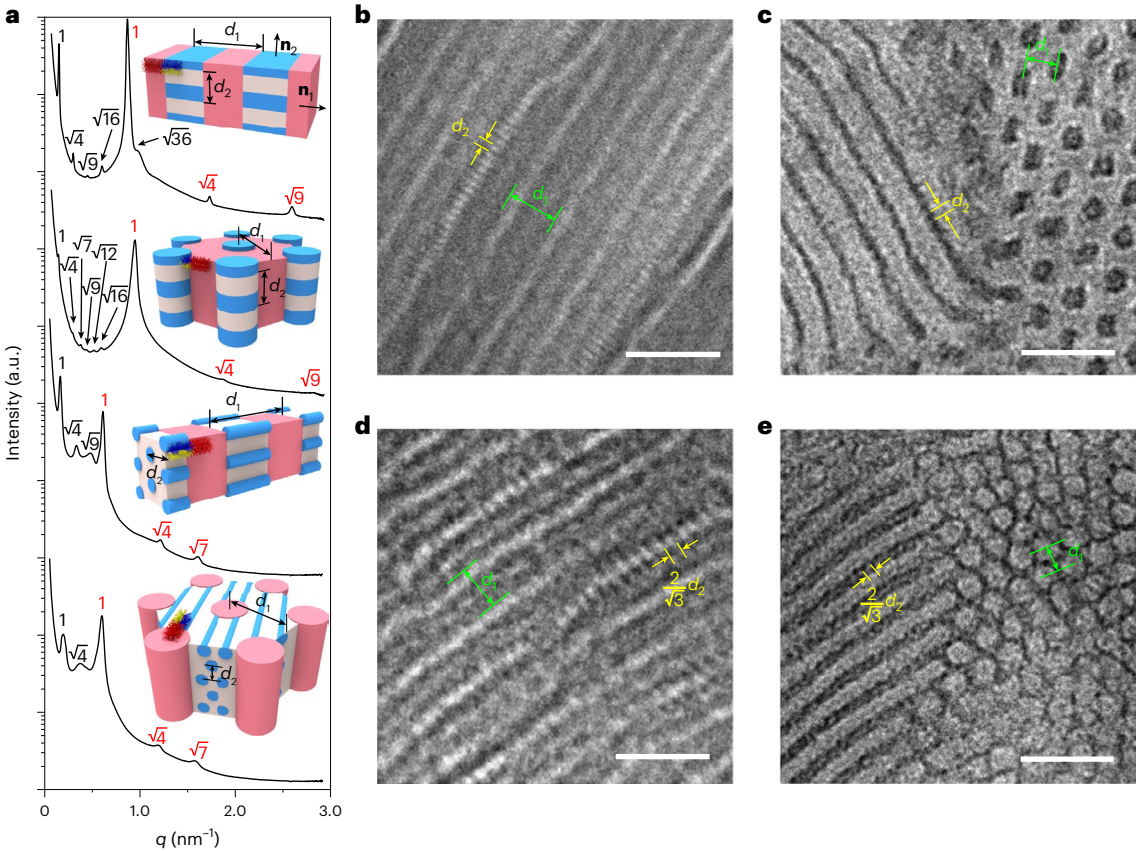

Fig. 2 | Hierarchical nanostructures constructed from (A-*alt*-B)-*b*-C-type GBCPs. a, Representative SAXS patterns and schematic illustrations for $(PDMS_m$-*alt*-$PLA_n)_x$-*b*-$(PS_r)_y$ GBCPs. From top to bottom, $(PDMS_{14}$-*alt*-$PLA_{16})_{40}$-*b*-$(PS_{26})_{40}$, $(PDMS_{14}$-*alt*-$PLA_{12})_{76}$-*b*-$(PS_{26})_{80}$, $(PDMS_{37}$-*alt*-$PLA_{20})_{35}$-*b*-$(PS_{26})_{40}$ and $(PDMS_{37}$-*alt*-$PLA_{20})_{22}$-*b*-$(PS_{26})_{30}$. The numbers in black and red correspond to the indices of the superstructures and substructures, respectively. All samples were tested after annealing at 130 °C for 10 h, followed by 80 °C for 10 h. **b**–**e**, TEM images of GBCPs corresponding to samples listed from top to bottom, respectively, in **a**. Scale bars, 100 nm.

Hierarchical assembly of CAMBBs

The hypothesized hierarchical assembly of $(PDMS_m$-*alt*-$PLA_n)_x$-*b*-$(PS_r)_y$, where the subscripts *m*, *n* and *r* in the parentheses represent the degrees of polymerization of the corresponding side chains, was studied and validated by small angle X-ray scattering (SAXS) in reciprocal space and transmission electron microscopy (TEM) in real space. The SAXS patterns of all $(PDMS_m$-*alt*-$PLA_n)_x$-*b*-$(PS_r)_y$ in this study displayed reflections from two sets of lattices that were respectively indexed in red and black (Fig. 2a). The red indices with scattering vector magnitude *q* ratios of $1{:}\sqrt{4}{:}\sqrt{9}$ in both $(PDMS_{14}$-*alt*-$PLA_{16})_{40}$-*b*-$(PS_{26})_{40}$ and $(PDMS_{14}$-*alt*-$PLA_{12})_{76}$-*b*-$(PS_{26})_{80}$ originated from their (PDMS-*alt*-PLA) blocks that formed lamellar substructures with spatial periodicities (that is, *d* spacings), of 7.3 nm and 6.6 nm, respectively. The (PDMS-*alt*-PLA) block itself phase-separated with the PS block, resulting in a superstructure lattice as revealed by the black indices. The $(PDMS_{14}$-*alt*-$PLA_{16})_{40}$-*b*-$(PS_{26})_{40}$ with a PS volume fraction (f_{PS}) of 0.54 provided a lamellar superstructure morphology (*q* ratios = $1{:}\sqrt{4}{:}\sqrt{9}{:}\sqrt{16}{:}\sqrt{36}$) with a *d* spacing of 41.6 nm. The $(PDMS_{14}$-*alt*-$PLA_{12})_{76}$-*b*-$(PS_{26})_{80}$ with a slightly increased f_{PS} of 0.55 resulted in a superstructure comprising (PDMS-*alt*PLA)-based cylinders that are hexagonally distributed in a continuous PS matrix (*q* ratios = $1{:}\sqrt{4}{:}\sqrt{7}{:}\sqrt{9}{:}\sqrt{12}{:}\sqrt{16}$) with an inter-cylinder distance (*D*) of 52.4 nm. The morphological transition of the superstructure from lamellae to cylinders with such a subtle change in f_{PS} could be ascribed to the lateral asymmetry of the GBCP that was introduced when the degree of polymerization of the PLA side chain decreased from 16 to 12 (ref. [24]). These phase-*in*-phase morphologies, that is, lamellae-*in*-lamellae and lamellae-*in*-cylinders, were confirmed by dissipative particle dynamics (DPD) simulations (Supplementary Figs. 1 and 2) and visualized by TEM of the microtomed thin-sectioned samples (Fig. 2b,c). The contrast between PDMS and PLA in the substructure, particularly for the sample with a lamellae-*in*-cylinders morphology, was enhanced through RuO_4 staining (Supplementary Figs. 46 and 47), though the contrast between PS and PLA was compromised, and over-staining of PS and PLA proved to be necessary in order to achieve sufficiently large contrast in the substructures. The TEM images obtained from RuO_4-stained samples provided direct evidence that the substructure and superstructure lattices are orthogonally oriented. In the lamellae-*in*-lamellae morphology, the surface normal vectors of the superstructures ($\mathbf{n_1}$) and substructures ($\mathbf{n_2}$) are orthogonal (Fig. 2a). For a fixed orientation of the superstructure, the substructure has a degenerate arrangement as $\mathbf{n_2}$ can lie at any angle in the plane perpendicular to $\mathbf{n_1}$. These degenerate orientation states, obtained in the same morphology by DPD simulations (Supplementary Fig. 1), led to the coexistence of PDMS-PLA stripes with and without layered substructure features in the same local area (Fig. 2b and Supplementary Fig. 48). Lamellar substructures in some PDMS-PLA domains were not visible in TEM when $\mathbf{n_2}$ was along the viewing direction.

To diversify the hierarchical nanostructures constructed from CAMBBs, $(PDMS_{37}$-*alt*-$PLA_{20})_x$-*b*-$(PS_{26})_y$ GBCPs containing a cylinder-forming (PDMS-*alt*-PLA) block were synthesized. The $(PDMS_{37}$-*alt*-$PLA_{20})_{35}$-*b*-$(PS_{26})_{40}$ containing an asymmetric Janus (PDMS-*alt*-PLA) block created a cylinders-*in*-lamellae morphology

https://doi.org/10.1038/s41563-022-01393-0

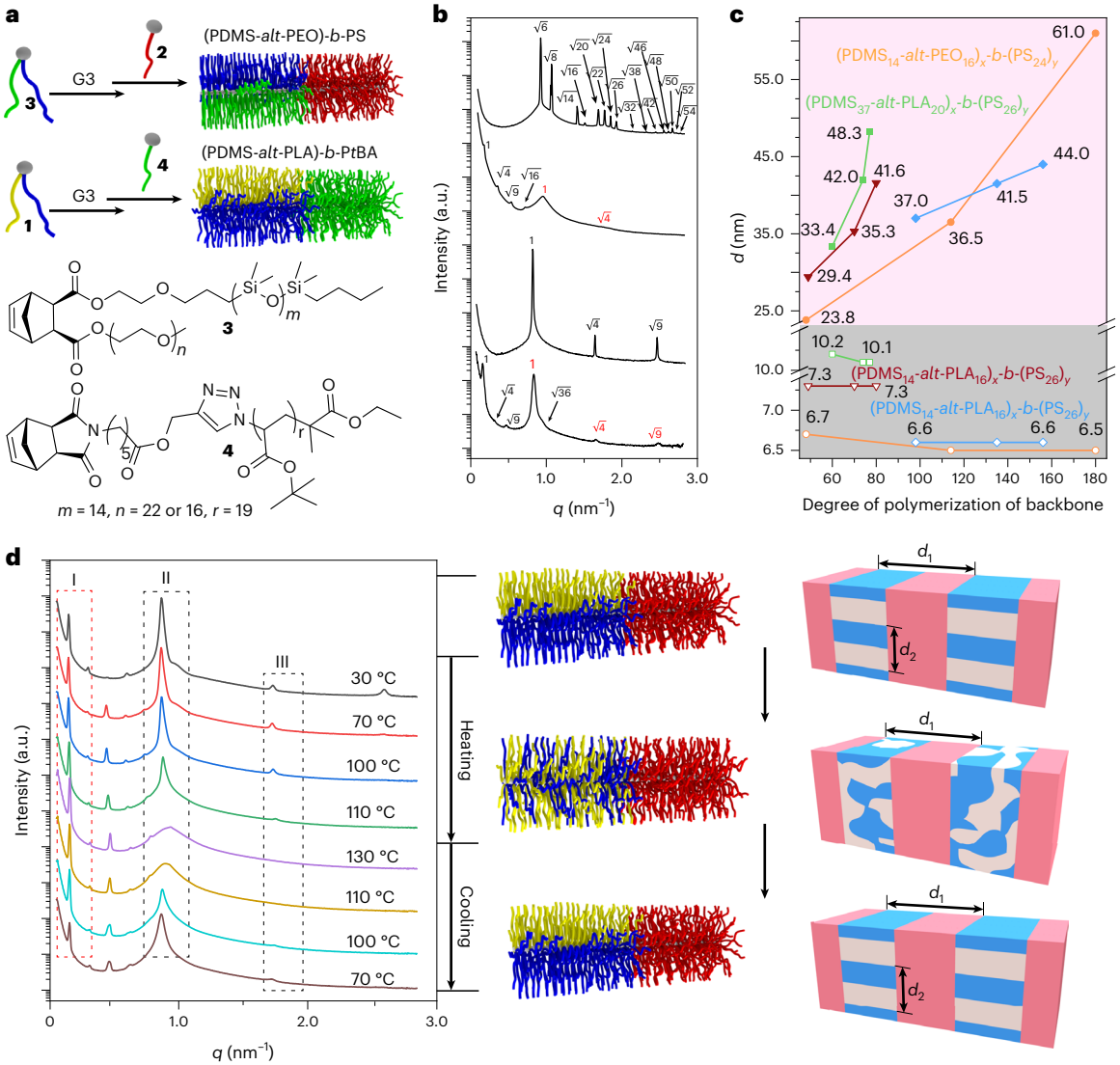

Fig. 3 | Diversity of side-chain compositions of (A-*alt*-B)-*b*-C-type GBCPs and independent tunability between superstructure and substructure. **a**, Schemes of the synthesis of (A-*alt*-B)-*b*-C GBCPs using various polymer side chains. **b**, Representative SAXS patterns of (A-*alt*-B)-*b*-C GBCPs with diverse side-chain compositions and corresponding parent Janus GBCPs. From top to bottom, $(PDMS_{14}\text{-}alt\text{-}PEO_{16})_{50}$, $(PDMS_{14}\text{-}alt\text{-}PEO_{16})_{64}\text{-}b\text{-}(PS_{24})_{50}$, $(PDMS_{14}\text{-}alt\text{-}PLA_{16})_{50}$ and $(PDMS_{14}\text{-}alt\text{-}PLA_{16})_{30}\text{-}b\text{-}(PtBA_{19})_{25}$. The numbers in black and red correspond to the indices of the superstructure and substructure, respectively. **c**, The *d* spacings of the superstructure (pink region) and substructure (grey region) as a function of the overall backbone degree of polymerization, that is, $x + y$. **d**, Temperature-resolved SAXS profiles of $(PDMS_{14}\text{-}alt\text{-}PLA_{16})_{40}\text{-}b\text{-}(PS_{26})_{40}$ and schematic representation of the reversible order-to-disorder transition in the substructure during the heating–cooling cycle. The regions I, II and III are explained in the main text.

(Fig. 2a,d). The layered substructure within the superstructure can be assigned to the lying-down PLA cylinders that are perpendicular to the interfaces of PS and (PLA-*alt*-PDMS). Missing substructure features in some (PDMS-*alt*-PLA)-rich domains (Fig. 2d and Supplementary Figs. 51 and 52) can be attributed to the orientational degeneracy of the cylindrical lattice, as rationalized by DPD simulations (Supplementary Fig. 3). The combined information from SAXS and TEM (Fig. 2a,e) suggested that a cylinders-*in*-cylinders morphology was obtained in $(PDMS_{37}\text{-}alt\text{-}PLA_{20})_{22}\text{-}b\text{-}(PS_{26})_{30}$. While it was difficult to determine, through TEM, the relative orientation of the PLA subcylinders that were embedded in the continuous matrix rich in PDMS and PLA, DPD simulations indicated that the constraint of the PS cylinders could result in different possible normal orientations of the PLA subcylinders (Supplementary Figs. 4 and 5).

GBCPs incorporated with other types of polymer side chains exhibited a similar phase behaviour and hierarchical assembly. Replacing PLA with poly(ethylene oxide) (PEO) (Fig. 3a, **3**) or PS with poly(*tert*-butyl acrylate) (P*t*BA) (Fig. 3a, **4**) yielded two new series of GBCPs: $(PDMS_{14}\text{-}alt\text{-}PEO_{16})_x\text{-}b\text{-}(PS_{24})_y$ and $(PDMS_{14}\text{-}alt\text{-}PLA_{16})_x\text{-}b\text{-}(PtBA_{19})_y$ (Fig. 3a). A lamellae-*in*-lamellae morphology was observed in both series of samples (Fig. 3b). The $(PDMS_{14}\text{-}alt\text{-}PEO_{16})_{64}\text{-}b\text{-}(PS_{24})_{50}$ formed a lamellar substructure despite the gyroid-forming parent (PDMS-*alt*-PEO) block, suggesting that a morphological change was required to minimize the interfacial energy in the phase-*in*-phase nanostructures. The hierarchically assembling GBCPs are compatible with varied chemical compositions and provide a robust platform for the future design of nanostructured materials integrating diverse functionalities.

Independently tailored superstructures and substructures

To highlight the unique design strategy of using GBCPs toward the preparation of hierarchically assembled nanostructures, *d* spacings in all prepared (A-*alt*-B)-*b*-C GBCPs were compared, as summarized

https://doi.org/10.1038/s41563-022-01393-0

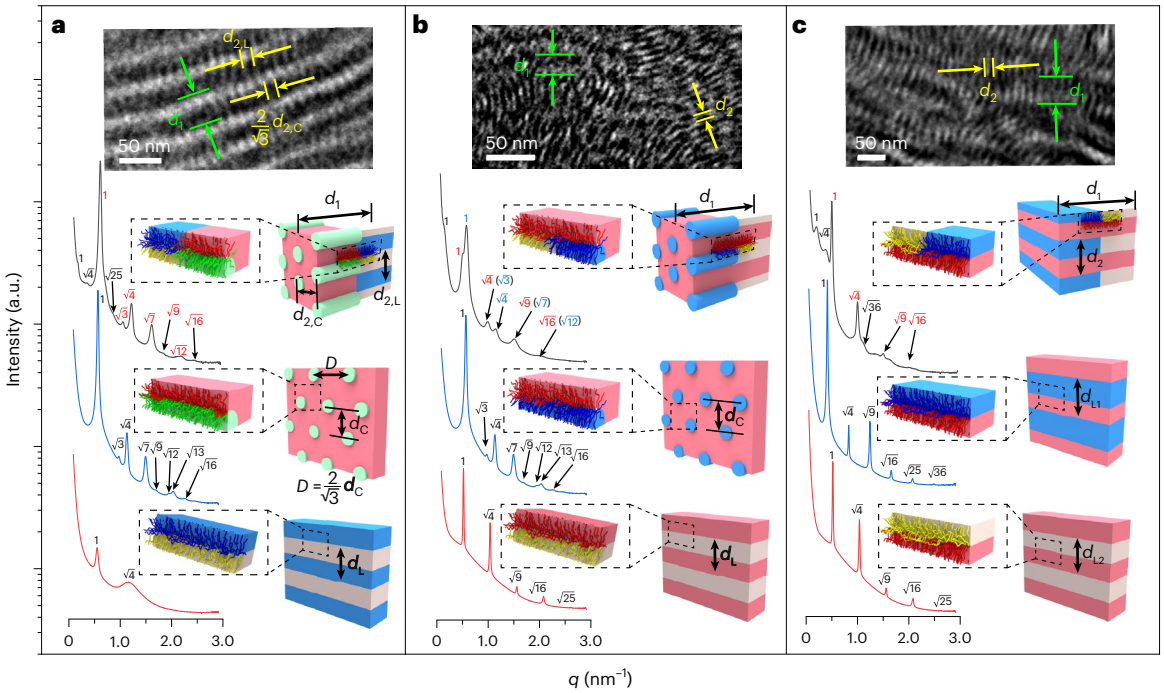

Fig. 4 | CAMBBs beyond (A-*alt*-B)-*b*-C-type GBCPs. TEM images and representative SAXS patterns for multi-block GBCPs and corresponding parent Janus GBCPs. **a**, (A-*alt*-B)-*b*-(C-*alt*-D). From top to bottom, $(PDMS_{37}$-*alt*-$PLA_{20})_{45}$-*b*-$(PS_{27}$-*alt*-$PtBA_{19})_{15}$, $(PDMS_{37}$-*alt*-$PLA_{20})_{45}$ and $(PS_{27}$-*alt*-$PtBA_{19})_{30}$. **b**, (A-*alt*-C)-*b*-(B-*alt*-C) with heterosubstructures. From top to bottom, $(PDMS_{37}$-*alt*-$PLA_{20})_{27}$-*b*-$(PDMS_{37}$-*alt*-$PS_{27})_{17}$, $(PDMS_{37}$-*alt*-$PLA_{20})_{45}$ and $(PDMS_{37}$-*alt*-$PS_{27})_{30}$. **c**, (A-*alt*-C)-*b*-(B-*alt*-C) containing two lamellae-forming Janus blocks. From top to bottom, $(PDMS_{37}$-*alt*-$PS_{27})_{40}$-*b*-$(PDMS_{37}$-*alt*-$PLA_{81})_{15}$, $(PDMS_{37}$-*alt*-$PLA_{81})_{30}$ and $(PDMS_{37}$-*alt*-$PS_{27})_{30}$.

in Fig. 3c. In the series of GBCPs synthesized from the same macromonomers, the *d* spacing of the superstructure was defined by the backbone degree of polymerization, and therefore could be readily tuned by adjusting the backbone length of one or both of the blocks. Hence, the *d* spacing of the superstructure was increased almost linearly with the increase in the degree of polymerization of the GBCP backbone (Fig. 3c, pink region). By contrast, the characteristic length of the substructure remained unchanged (Fig. 3c, grey region). For instance, in the $(PDMS_{14}$-*alt*-$PLA_{16})_x$-*b*-$(PS_{26})_y$ series with a superstructure *d* spacing ranging from 29.4 nm to 41.6 nm, a constant *d* spacing of 7.3 nm in the lamellar substructure was maintained, even after a morphological transition from lamellae to cylinders occurred in the superstructure (Supplementary Fig. 63 and Supplementary Table 2). This independent tunability in the size of the different lattices, and thereby in the different orientations of the structure, is in contrast with the phase-*in*-phase nanostructures that were observed in other systems such as linear or mikto-arm multi-block copolymers as well as the supramolecular materials assembled through complexation of mesogenic moieties or hydrogen bonding. In these previously reported materials, two sets of lattice parameters were mutually determined by the overall composition and lengths of all blocks and could not be decoupled from one another[29–34]. A $(PS_{78})_{100}$-*b*-$(PDMS_{37}$-*alt*-$PLA_{20})_{100}$ GBCP was also synthesized with a long backbone extending the *d* spacing of the superstructure to the mesoscale range (d_1 = 105.1 nm), while the substructure (d_2 = 10.6 nm) was maintained in the nanoscale range (Supplementary Fig. 77).

The relationship between substructure and superstructure lattices was further studied under a dynamic environment using temperature-resolved SAXS (Fig. 3d). During the heating–cooling cycle within the temperature range of 30–130 °C, the superstructure of $(PDMS_{14}$-*alt*-$PLA_{16})_{40}$-*b*-$(PS_{26})_{40}$ was maintained intact in an ordered state (Fig. 3d, region I) due to a relatively high order-to-disorder transition temperature (T_{ODT}) above 130 °C. On the other hand, the PDMS-PLA substructure underwent a reversible order-to-disorder transition, as evidenced by the disappearance and reappearance of a higher order peak (Fig. 3d, region III) accompanied by the broadening and narrowing of the primary peak (Fig. 3d, region II). The order-to-disorder transition of the substructure took place at around 110 °C—a similar T_{ODT} to that observed in the Janus $(PDMS_{14}$-*alt*-$PLA_{16})_x$ GBCP[27], suggesting that the superstructure formation had minimal impact on the order-to-disorder transition of the Janus block.

Formation of heterosubstructures

The scope of the hierarchical phase-*in*-phase nanostructures was expanded by introducing two distinct branched macromonomers in the GBCP synthesis. An (A-*alt*-B)-*b*-(C-*alt*-D)-type GBCP, $(PDMS_{37}$-*alt*-$PLA_{20})_{45}$-*b*-$(PS_{27}$-*alt*-$PtBA_{19})_{15}$, was synthesized through the sequential ROMP of Nb-$(PDMS_{37}$-*branch*-$PLA_{20})$ and Nb-$(PS_{27}$-*branch*-$PtBA_{19})$ (Supplementary Scheme 12). The annealed sample displayed a lamellar superstructure (Fig. 4a) with interfaces dividing the PDMS-PLA and PS-P*t*BA domains. An alternating lamellar-cylindrical substructure was hypothesized based on the fact that the two parent Janus blocks $(PDMS_{37}$-*branch*-$PLA_{20})_x$ and $(PS_{27}$-*branch*-$PtBA_{19})_y$ formed cylindrical (d_C = 11.2 nm) and lamellar (d_L = 11.4 nm) morphologies, respectively (Fig. 4a). While the lamellar features were missing in the SAXS profile due to the lower electron density contrast of PS and P*t*BA compared to that of PDMS and PLA, TEM images with layered substructures observed in both the PDMS-PLA and PS-P*t*BA domains further supported our hypothesis (Fig. 4a). In the self-assembly, the cylinder-forming (PDMS-*alt*-PLA) block with a slightly larger lateral size shrank to match its inter-cylinder distance D ($D = \sqrt{4/3}d_C$) with $d_{2,L}$ in the PS-P*t*BA domain. Thus, a decreased *d* spacing for the cylindrical substructure ($d_{2,C}$) of 10.3 nm (D = 11.8 nm) was obtained in the PDMS-PLA domain of the quaternary GBCP.

The formation of heterosubstructures in an (A-*alt*-B)-*b*-(C-*alt*-D)-type GBCP has less stringent constraints in regard to the

lattice matching than that in an (A-*alt*-C)-*b*-(B-*alt*-C)-type GBCP where the same C side chains are shared by both the (A-*alt*-C) and (B-*alt*-C) blocks. Due to the mutual C side chains in both blocks, a d_L/d_C ratio of 1.15 is required to construct a non-frustrated alternating lamellar-cylindrical substructure in a space-filling morphology (Supplementary Fig. 74). The $(PDMS_{37}\text{-}alt\text{-}PLA_{20})_{27}$-*b*-$(PDMS_{37}\text{-}alt\text{-}PS_{27})_{17}$ was prepared containing a cylinder-forming $(PDMS_{37}\text{-}alt\text{-}PLA_{20})_x$ block (d_C = 11.2 nm) and a lamellae-forming $(PDMS_{37}\text{-}alt\text{-}PS_{27})_y$ block (d_L = 12.1 nm; Fig. 4b), giving a d_L/d_C ratio of 1.08 as calculated from the parent blocks. The SAXS pattern presented three sets of lattice indices, two of which resided in the substructure region with clearly identified lamellar and cylindrical features because of the large contrast of electron density in both silicon-rich Janus blocks (Fig. 4b). To match the optimal d_L/d_C ratio in the ternary GBCP, PDMS-PLA and PDMS-PS substructures respectively shrank and expanded compared to the parent binary GBCPs, resulting in an adapted d_L/d_C ratio of 1.16 (Supplementary Table 2). In spite of the well-resolved substructure features, the degree of ordering in the superstructure was sacrificed due to the frustrated side-chain packing in both blocks.

An (A-*alt*-C)-*b*-(B-*alt*-C)-type GBCP containing both lamellae-forming (A-*alt*-C) and (B-*alt*-C) blocks has a higher tolerance for mismatched side-chain lengths, compared to the aforementioned (A-*alt*-C)-*b*-(B-*alt*-C) with heterosubstructures. An ordered lamellae-*in*-lamellae morphology was realized in an (A-*alt*-C)-*b*-(B-*alt*-C)-type GBCP with a relatively large discrepancy between the lateral sizes of the two lamellae-forming blocks. In this GBCP with a composition of $(PDMS_{37}\text{-}alt\text{-}PS_{27})_{40}$-*b*-$(PDMS_{37}\text{-}alt\text{-}PLA_{81})_{15}$, merging the lamellar $(PDMS_{37}\text{-}alt\text{-}PLA_{81})_x$ (d_{L1} = 15.0 nm) and lamellar $(PDMS_{37}\text{-}alt\text{-}PS_{27})_y$ (d_{L2} = 12.1 nm) resulted in a new shared lamellar substructure with a compromised *d* spacing of 12.5 nm as well as a relatively ordered lamellar superstructure (Fig. 4c). This assembly process that involved frustrated chain packing inevitably produced layered substructures with large undulations in some local areas (Supplementary Figs. 75 and 76) to release the unbalanced interfacial energy.

The GBCP-based CAMBBs accessed a series of phase-*in*-phase hierarchical structures. These complex structures, assembled from a single molecular building block, presented more than one type of periodic structural feature with independently tunable periodicities across nanoscopic and mesoscopic length scales. A diverse variety of organic components can be integrated into these hierarchical structures for the fabrication of multifunctional materials.

Online content

Any methods, additional references, Nature Research reporting summaries, source data, extended data, supplementary information, acknowledgements, peer review information; details of author contributions and competing interests; and statements of data and code availability are available at https://doi.org/10.1038/s41563-022-01393-0.

References

1. Garnier, F., Hajlaoui, R., Yassar, A. & Srivastava, P. All-polymer field-effect transistor realized by printing techniques. *Science* **265**, 1684–1686 (1994).
2. Sirringhaus, H. et al. High-resolution inkjet printing of all-polymer transistor circuits. *Science* **290**, 2123–2126 (2000).
3. Stoykovich, M. P. et al. Directed assembly of block copolymer blends into nonregular device-oriented structures. *Science* **308**, 1442–1446 (2005).
4. Huo, F. et al. Polymer pen lithography. *Science* **321**, 1658–1660 (2008).
5. Tumbleston, J. R. et al. Continuous liquid interface production of 3D objects. *Science* **347**, 1349–1352 (2015).
6. Zeng, C., Chen, Y., Kirschbaum, K., Lambright, K. J. & Jin, R. Emergence of hierarchical structural complexities in nanoparticles and their assembly. *Science* **354**, 1580–1584 (2016).
7. Feng, L., Wang, K.-Y., Willman, J. & Zhou, H.-C. Hierarchy in metal–organic frameworks. *ACS Central Sci.* **6**, 359–367 (2020).
8. Lutz, J.-F., Lehn, J.-M., Meijer, E. W. & Matyjaszewski, K. From precision polymers to complex materials and systems. *Nat. Rev. Mater.* **1**, 16024 (2016).
9. Li, C. et al. Supramolecular–covalent hybrid polymers for light-activated mechanical actuation. *Nat. Mater.* **19**, 900–909 (2020).
10. Feng, X. et al. Single crystal texture by directed molecular self-assembly along dual axes. *Nat. Mater.* **18**, 1235–1243 (2019).
11. Macfarlane, R. J., Jones, M. R., Lee, B., Auyeung, E. & Mirkin, C. A. Topotactic interconversion of nanoparticle superlattices. *Science* **341**, 1222–1225 (2013).
12. Nagaoka, Y. et al. Superstructures generated from truncated tetrahedral quantum dots. *Nature* **561**, 378–382 (2018).
13. Tian, Y. et al. Ordered three-dimensional nanomaterials using DNA-prescribed and valence-controlled material voxels. *Nat. Mater.* **19**, 789–796 (2020).
14. Santos, P. J., Gabrys, P. A., Zornberg, L. Z., Lee, M. S. & Macfarlane, R. J. Macroscopic materials assembled from nanoparticle superlattices. *Nature* **591**, 586–591 (2021).
15. Hudson, S. D. et al. Direct visualization of individual cylindrical and spherical supramolecular dendrimers. *Science* **278**, 449–452 (1997).
16. Lee, S., Bluemle, M. J. & Bates, F. S. Discovery of a Frank-Kasper σ phase in sphere-forming block copolymer melts. *Science* **330**, 349–353 (2010).
17. Bates, F. S. et al. Multiblock polymers: panacea or Pandora's box? *Science* **336**, 434–440 (2012).
18. Huang, M. et al. Selective assemblies of giant tetrahedra via precisely controlled positional interactions. *Science* **348**, 424–428 (2015).
19. Bockstaller, M. R., Mickiewicz, R. A. & Thomas, E. L. Block copolymer nanocomposites: perspectives for tailored functional materials. *Adv. Mater.* **17**, 1331–1349 (2005).
20. Aldaye, F. A., Palmer, A. L. & Sleiman, H. F. Assembling materials with DNA as the guide. *Science* **321**, 1795–1799 (2008).
21. Zhao, Y. et al. Small-molecule-directed nanoparticle assembly towards stimuli-responsive nanocomposites. *Nat. Mater.* **8**, 979–985 (2009).
22. Sanford, M. S., Love, J. A. & Grubbs, R. H. A versatile precursor for the synthesis of new ruthenium olefin metathesis catalysts. *Organometallics* **20**, 5314–5318 (2001).
23. Xia, Y., Olsen, B. D., Kornfield, J. A. & Grubbs, R. H. Efficient synthesis of narrowly dispersed brush copolymers and study of their assemblies: the importance of side chain arrangement. *J. Am. Chem. Soc.* **131**, 18525–18532 (2009).
24. Bolton, J., Bailey, T. S. & Rzayev, J. Large pore size nanoporous materials from the self-assembly of asymmetric bottlebrush block copolymers. *Nano Lett.* **11**, 998–1001 (2011).
25. Chae, C.-G. et al. Experimental formulation of photonic crystal properties for hierarchically self-assembled POSS–bottlebrush block copolymers. *Macromolecules* **51**, 3458–3466 (2018).
26. Fei, H.-F. et al. Influence of molecular architecture and chain flexibility on the phase map of polystyrene-*block*-poly (dimethylsiloxane) brush block copolymers. *Macromolecules* **52**, 6449–6457 (2019).
27. Guo, Z. H. et al. Janus graft block copolymers: design of a polymer architecture for independently tuned nanostructures and polymer properties. *Angew. Chem. Int. Ed.* **57**, 8493–8497 (2018).
28. Kawamoto, K. et al. Graft-through synthesis and assembly of Janus bottlebrush polymers from A-*branch*-B diblock macromonomers. *J. Am. Chem. Soc.* **138**, 11501–11504 (2016).

29. Masuda, J. et al. Composition-dependent morphological transition of hierarchically-ordered structures formed by multiblock terpolymers. *Macromolecules* **40**, 4023–4027 (2007).
30. Hayashida, K. et al. Hierarchical morphologies formed by ABC star-shaped terpolymers. *Macromolecules* **40**, 3695–3699 (2007).
31. Markov, V., Kriksin, Y., Erukhimovich, I. & Brinke, G. T. Perpendicular lamellar-*in*-lamellar and other planar morphologies in A-*b*-(B-*b*-A)$_2$-*b*-C and (B-*b*-A)$_2$-*b*-C ternary multiblock copolymer melts. *J. Chem. Phys.* **139**, 084906 (2013).
32. Ruokolainen, J., Brinke, G. T. & Ikkala, O. Supramolecular polymeric materials with hierarchical structure-within-structure morphologies. *Adv. Mater.* **11**, 777–780 (1999).
33. Zhang, Z.-K. et al. Hierarchical structures with double lower disorder-to-order transition and closed-loop phase behaviors in charged block copolymers bearing long alkyl side groups. *Macromolecules* **53**, 8714–8724 (2020).
34. Hofman, A. H., Terzic, I., Stuart, M. C. A., ten Brinke, G. & Loos, K. Hierarchical self-assembly of supramolecular double-comb triblock terpolymers. *ACS Macro Lett.* **7**, 1168–1173 (2018).

Methods

A complete set of detailed synthetic procedures for organic small molecules and polymers and spectral data are available in the Supplementary Information.

Materials and instrumentation

All chemicals were used as received from Sigma-Aldrich, Acros Organics or Alfa Aesar, unless otherwise specified. American Chemical Society (ACS)-grade solvents were used as received from Sigma-Aldrich and Macron Fine Chemicals, unless otherwise specified. Neutral and basic aluminium oxide (Al_2O_3; standard activity I grade) were purchased from Sorbent Technologies with 50–200 μm particle size. All commercial monomers used in this work, including styrene and *tert*-butyl acrylate, were passed through a short column of basic Al_2O_3 to remove inhibitor prior to use. Monocarbinol terminated PDMS (that is, $PDMS_{14}$, number-average molecular weight M_n = 1,000 Da) was used as purchased from Gelest. $PDMS_{37}$ (M_n = 2,800 Da) was used as received from Shin-Etsu Silicones of America. PEO monomethyl ether (PEO_{16} and PEO_{22}; M_n = 750 Da and 1,000 Da, respectively) was used as purchased from TCI. High-performance liquid chromatography (HPLC)-grade anhydrous dichloromethane was obtained from a J. C. Meyer solvent purification system. Chromatography was performed using silica gel from Sorbtech with 60 Å porosity and 40–63 μm particle size on a Biotage Isolera Prime flash purification system. Preparative gel permeation chromatography (GPC) was performed on a LaboACE LC-5060 recycling preparative HPLC with refractive index and ultraviolet detectors, equipped with a JAIGEL-2.5HR column from Japan Analytical Industry, operating at a flow rate of 10 ml min^{-1} at room temperature. The solvent for the preparative GPC was HPLC-grade chloroform from J. T. Baker. Analytic GPC measurements were taken at a 0.1–1.0 mg ml^{-1} concentration in HPLC-grade tetrahydrofuran (J. T. Baker) on a TOSOH Bioscience EcoSEC HKC08320GPC with a differential refractive index detector, equipped with a TSKgel GMHHR-M column. The GPC was run at a flow rate of 1 ml min^{-1} at 40 °C, and the instrument was calibrated using linear polystyrene standards. Proton nuclear magnetic resonance (^{1}H NMR) spectra were recorded on an Agilent DD2 400 MHz or 600 MHz NMR spectrometer with 10 s relaxation time. Chemical shifts are reported in parts per million (ppm) using solvent resonance as the internal standard ($CDCl_3$, 7.26 ppm; CD_2Cl_2, 5.32 ppm). NMR spectra were processed using MestReNova v.14.2.0. SAXS and differential scanning calorimetry data were processed using Origin 2020. TEM imaging was performed on an FEI Tecnai Osiris 200 kV TEM instrument. TEM images were analysed using the ImageJ program.

General ROMP procedures for the GBCP syntheses

ROMP reactions were performed in a glove box at ambient temperature using 2 ml glass vials and Teflon magnetic stir bars. Branched and linear macromonomers were thoroughly dried under vacuum prior to reaction in order to obtain accurate masses and solution concentrations. Macromonomers were dissolved in anhydrous dichloromethane in the glove box; 20–50 mM concentrations were targeted. The macromonomer solution was transferred into the 2 ml glass vials in the appropriate amounts using a 1 ml syringe. The added macromonomers were assumed to contribute a negligible volume to the solution. To use the G3 catalyst for ROMP, a portion of the catalyst was dissolved to 2–10 mM using anhydrous tetrahydrofuran. The catalyst solution was then dispensed into vials containing previously measured macromonomer solution to obtain the desired ratio of macromonomer to G3 initiator ratio. The reaction materials were stirred for 40 min, and then another macromonomer for the second backbone block was added to react for another 40 min. The reaction mixture was removed from the glove box and quenched with excess ethyl vinyl ether. The metal catalyst was removed by passing the product solution through a neutral alumina column, and the product was purified by preparative GPC. Each sample was characterized by analytical GPC with tetrahydrofuran as the eluent and by ^{1}H NMR to characterize the volume fraction of each component. The detailed chemical structure of the GBCPs is in Supplementary Schemes 11 and 12. The component information of all the GBCPs is summarized in Supplementary Tables 1 and 2. GPC traces of the GBCPs and corresponding precursors are shown in Supplementary Figs. 11–44.

TEM sample preparation and measurement

Thermally annealed samples (130 °C for 10 h, then 80 °C for 10 h) were embedded in EPON resin, cured at 60 °C and then sectioned at ambient temperature to 70–90 nm thickness using a Leica EM UC7 ultramicrotome equipped with a diamond knife (DiaTOME). Sections were transferred onto carbon-coated copper grids for TEM imaging. In a general staining procedure, the copper grids were placed in a glassy Petri dish under the vapour of an 0.5% RuO_4 aqueous solution for 15 min, washed with deionized water and then dried under vacuum. TEM images of the GBCP samples are provided in Supplementary Figs. 45–60.

SAXS sample preparation and measurement

Samples for SAXS were filled into the hole of a circular washer that acted as a sample holder (outer diameter, 24 mm; inner diameter, 2 mm; thickness, 1 mm). For liquid samples, a layer of Kapton tape was attached to either side of the washer containing the sample. Samples were then placed in a vacuum oven, evacuated and heated to 100 or 130 °C for 8 h. The vacuum oven was allowed to cool overnight to ambient temperature and then vented to the atmosphere. Transmission SAXS was conducted using the CMS beamline (11-BM) at Brookhaven National Laboratory. The beamline was configured with an X-ray wavelength of 0.932 Å. The two-dimensional scattering patterns were azimuthally integrated into one-dimensional plots of scattering intensity (I) versus the magnitude of the scattering vector (q), where $q = 4\pi\sin\theta/\lambda$, λ is the wavelength and the scattering angle is 2θ. SAXS profiles of the GBCP samples are provided in Supplementary Figs. 61–83.

Differential scanning calorimetry measurement

Differential scanning calorimetry was performed using a DSC2500 (TA Instruments) at a heating or cooling rate of 10 °C min^{-1}. Differential scanning calorimetry profiles of the GBCP samples are provided in Supplementary Figs. 84 and 85.

Simulation method and model

Simulations were performed with the GALAMOST (v.4.0.1) simulation package[35], using the DPD method, in the canonical ensemble. The DPD method is a coarse-grained particle-based mesoscopic simulation technique that was introduced by Hoogerbrugge and Koelman in 1992 (ref. [36]). The coarse-graining approach was employed to overcome the time and space scale limitation encountered in molecular dynamics simulations. It was able to capture universal properties of polymers rather than the interactions between specific chemical functional groups. The time evolution of DPD beads with unit mass is governed by Newton's equations[37] of motion:

$$\frac{d\mathbf{r}_i}{dt} = \mathbf{v}_i, \frac{d\mathbf{v}_i}{dt} = \mathbf{f}_i \quad (1)$$

$$\mathbf{f}_i = \sum_{j \neq i} \left(\mathbf{F}_{ij}^{C} + \mathbf{F}_{ij}^{D} + \mathbf{F}_{ij}^{R} \right) \quad (2)$$

in which $\mathbf{f}_i$ is the force applied on particle i and composed of conservative force $\mathbf{F}_{ij}^{C}$, dissipative force $\mathbf{F}_{ij}^{D}$ and random force $\mathbf{F}_{ij}^{R}$. $\mathbf{r}_i$, $\mathbf{v}_i$ and t are the position, velocity and motion time of particle i, respectively. r_c is the cutoff radius. All forces are pairwise additive, short range and repulsive, and are cut at $r_c = 1$.

The conservative force $\mathbf{F}_{ij}^{C}$ is a soft-repulsive interaction acting along the line of the centres of two particles:

$$\mathbf{F}_{ij}^{C} = \begin{cases} a_{ij}(1 - r_{ij})\hat{\mathbf{r}}_{ij} & (r_{ij} < 1) \\ 0 & (r_{ij} \geqslant 1) \end{cases} \quad (3)$$

where $\mathbf{r}_{ij}$ is the vector pointing from j to i, and r_{ij} denotes the distance between beads i and j

$$\mathbf{r}_{ij} = \mathbf{r}_i - \mathbf{r}_j,\ r_{ij} = |\mathbf{r}_{ij}| \quad (4)$$

and $\hat{\mathbf{r}}_{ij}$ represents the unit vector pointing from j to i

$$\hat{\mathbf{r}}_{ij} = \mathbf{r}_{ij}/|\mathbf{r}_{ij}|. \quad (5)$$

The interaction parameter a_{ij} can be estimated from the Flory–Huggins parameter, χ, by $a_{ij} \approx 25 + 3.27\chi_{ij}$, according to Groot and Warren[37]. In other words, a_{ij} was chosen to be 25 between beads with the same type, or higher between different types of beads, due to the immiscibility. The PS monomer was modelled as bead A, the PDMS monomer as bead B and the PLA monomer as bead C (Supplementary Fig. 7). To qualitatively mimic the immiscibility between different types of monomers in the current system, we set $a_{AB} = a_{AC} = \frac{a_{BC}}{3} = 50$. No interaction was set between backbone beads and side-chain beads; thus, the backbone beads do not contribute to the calculation of the volume fractions.

The dissipative force $\mathbf{F}_{ij}^{D}$ is proportional to the relative velocity and takes the form

$$\mathbf{F}_{ij}^{D} = -\gamma w^{D}(r_{ij})(\hat{\mathbf{r}}_{ij}\mathbf{v}_{ij})\hat{\mathbf{r}}_{ij} \quad (6)$$

where $\mathbf{v}_{ij} = \mathbf{v}_i - \mathbf{v}_j$ is the relative velocity and γ is the friction coefficient governing the magnitude of the dissipative drag force.

The random force $\mathbf{F}_{ij}^{R}$ acts as a heat source to equilibrate the thermal motion of unresolved scales and takes the form

$$\mathbf{F}_{ij}^{R} = \sigma w^{R}(r_{ij})\theta_{ij}\hat{\mathbf{r}}_{ij} \quad (7)$$

where σ is the noise level controlling the intensity of the random force and is set to be 3. The $\theta_{ij}(t)$ is a randomly fluctuating variable with zero mean and unit variance. It satisfies Gaussian statistics:

$$\begin{aligned} &\langle\theta_{ij}(t)\rangle = 0, \\ &\langle\theta_{ij}(t)\theta_{kl}(t')\rangle = (\delta_{ik}\delta_{jl} + \delta_{il}\delta_{jk})\delta(t - t') \end{aligned} \quad (8)$$

where the δ variables are the Dirac delta functions, and t' denotes the time at the moment of t'. The random force is related to the dissipative force so that they satisfy the fluctuation–dissipation relation

$$\begin{aligned} &^{2} = 2\ \mathrm{k_B T}, \\ &\mathrm{w^D(r)} = \left[\mathrm{w^R(r)}\right]^2 = \begin{cases} (1 - \mathrm{r})^2 & (\mathrm{r} < 1) \\ 0 & (\mathrm{r} \geqslant 1) \end{cases} \end{aligned} \quad (9)$$

where w^{D} and w^{R} are the r-dependent weight functions vanishing at $r > r_c = 1$, T is temperature and k_B is the Boltzmann constant. Both the dissipative force and the random force act along the line of centres so that the linear and angular momentums are conservative, ensuring the simulation is performed in a canonical ensemble.

The beads on the polymeric chains are connected by a harmonic spring potential as

$$V_{\mathrm{bond}}(r) = \frac{1}{2}k_b r_b^2 \quad (10)$$

where r_b is the distance between connected beads and k_b is the spring constant and was chosen to be 4 according to Groot and Madden[38].

We qualitatively mimicked the stiffness of bonds in the backbone by imposing a cosine angle potential between two adjacent bonds:

$$V_{\mathrm{angle}}(\theta) = k_a[1 - (\cos\theta - \theta_0)] \quad (11)$$

where θ_0 is the equilibrium angle and was set to be π, θ is the angle between two neighbouring bonds and k_a is the potential constant. Since the stiffness is dependent on the grafting density, we set $k_a = 2$ for the PS-grafted backbone and $k_a = 12$ for the PDMS/PLA-grafted backbone in samples 1, 2 and 3 in Supplementary Tables 16. For sample 4 in Supplementary Tables 17, the variable stiffness was set to investigate the orientation of the cylinder substructure (Supplementary Figs. 8–10). The details about the grafting numbers and the number of beads on each side chain are provided in Supplementary Tables 3 and 4. While spheres-containing nanostructures were not easily identified experimentally due to the large packing frustration, DPD simulations suggest that the diversity of the hierarchical morphologies can be further expanded through tuning the backbone asymmetry and stiffness of the two blocks (Supplementary Fig. 6).

The number density of beads was fixed at 3 by setting the total number of polymeric chains as well as the sizes of the simulation box. The system temperature was maintained at $T^* = 1.0$. The radius of interaction and the particle mass m_p were set to unity, and the reduced unit of dimensionless time of the system was $\tau = r_c\sqrt{m_p/k_B T}$. The Velocity–Verlet integration scheme was used to integrate the equations of motion. The time step was set to be 0.01τ to achieve a balance between simulation stability and performance.

The GBCP molecules were randomly placed in the simulation box and were simulated for $(2 \times 10^4)\tau$ to generate a disordered state. Simulations of $(4.0 \times 10^5)\tau$ were performed to anneal each sample towards the equilibrium morphology.

Data availability

The data that support the findings of this study are available from the corresponding authors upon reasonable request. Source data are provided with this paper.

Code availability

The code generated during the current study is available from the corresponding authors upon reasonable request.

References

35. Zhu, Y.-L. et al. GALAMOST: GPU-accelerated large-scale molecular simulation toolkit. *J. Comput. Chem.* **34**, 2197–2211 (2013).
36. Hoogerbrugge, P. J. & Koelman, J. M. V. A. Simulating microscopic hydrodynamic phenomena with dissipative particle dynamics. *Europhys. Lett.* **19**, 155–160 (1992).
37. Groot, R. D. & Warren, P. B. Dissipative particle dynamics: bridging the gap between atomistic and mesoscopic simulation. *J. Chem. Phys.* **107**, 4423–4435 (1997).
38. Groot, R. D. & Madden, T. J. Dynamic simulation of diblock copolymer microphase separation. *J. Chem. Phys.* **108**, 8713–8724 (1998).

Acknowledgements

M.Z. acknowledges support from the National Science Foundation (NSF; DMR-2003875). J.A.J. acknowledges support from Eni S.p.A. through the MIT Energy Initiative and an NSF award (CHE-1629358). C.O.O. acknowledges support from an NSF award (DMR-1945966). W.L. acknowledges support from the National Natural Science Foundation of China (21925301). X.F. thanks the China Scholarship Council (CSC no. 201706240130) for the financial support for his visit at Yale University. A.N.L. thanks the NSF Graduate Research Fellowship for supporting her research. The research used resources of the CMS beamline (11-BM) of the National Synchrotron Light Source II, a US Department of Energy Office of Science User Facility operated for the US Department of Energy Office of Science by Brookhaven National Laboratory under

contract no. DE-SC0012704. We also thank R. Li (Brookhaven National Laboratory) and B. Q. Mercado (Yale) for their technical assistance with SAXS measurements during the COVID-19 pandemic.

Author contributions

R.L., Y.X., X.F., J.A.J. and M.Z. designed the research. R.L., Y.X. and X.F. performed all synthetic work; R.L., Y.X., X.F., A.N.L, Z.S. and R.D. conducted the structure and property characterization; Q.S., Y.Q., Q.X. and W.L. conducted the DPD simulations; and R.L., Y.X., X.F. and M.Z. analysed the data. R.L., Y.X., X.F., A.N.L., C.O.O., J.A.J., W.L. and M.Z. wrote the paper.

Competing interests

The authors declare no competing interests.

Additional information

Supplementary information The online version contains supplementary material available at https://doi.org/10.1038/s41563-022-01393-0.

Correspondence and requests for materials should be addressed to Jeremiah A. Johnson or Mingjiang Zhong.

Peer review information *Nature Materials* thanks the anonymous reviewers for their contribution to the peer review of this work.